2D Materials

Polarization-sensitive photoresponse in few-layer ZrSe3 photodetectors

Pedro L Alcázar Ruano[1,2] (ID), Daniel Vaquero[3], Estrella Sánchez Viso[1] (ID), Hao Li[1], Federico Mompeán[1], Francisco Domínguez-Adame[2], Andres Castellanos-Gomez[1] (ID) and Jorge Quereda[1,*]

1 2D Foundry group. Instituto de Ciencia de Materiales de Madrid (ICMM-CSIC), E-28049 Madrid, Spain
2 GISC, Departamento de Física de Materiales, Universidad Complutense, E-28040 Madrid, Spain
3 Zernike Institute for Advanced Materials, University of Groningen, 9747 AG Groningen, The Netherlands
* Author to whom any correspondence should be addressed.

E-mail: j.quereda@csic.es

Abstract

We present an in-depth spectral characterization of the fundamental optical and optoelectronic properties of few-layer $ZrSe_3$, a layered semiconductor of the group IV–V transition metal trichalcogenide family known for its in-plane anisotropic structure and quasi-1D electrical and optical characteristics. Our comprehensive analysis, conducted at both room temperature and in cryogenic vacuum, reveals that $ZrSe_3$ exhibits pronounced excitonic features in its optical spectra, which are highly sensitive to light polarization. These features are also evident in photocurrent spectra, presenting a strongly dichroic photoresponse with dichroic ratios exceeding 4 for excitation on resonance with the main exciton level. By comparing optical and optoelectronic spectral measurements, we elucidate the contributions of optically generated excitons to photocurrent. This work addresses substantial gaps of information in earlier literature for $ZrSe_3$ and advances the understanding of its unique symmetry and optical properties, paving the way for its application in nonlinear optoelectronic devices.

1. Introduction

In the last decade, two-dimensional (2D) materials have proven to be a revolutionary platform for the realization of ultrathin and ultralight optoelectronics [1–4]. These materials hold the promise to bring new functionalities and applications such as stronger light–matter interaction, flexibility, and transparency, while still being easily integrable with current CMOS technology. To date, the most deeply studied atomically thin semiconductors are Mo- and W-based transition metal dichalcogenides (TMDs), i.e. MoS_2, $MoSe_2$, WS_2 or WSe_2 [5–7], mainly because they have reasonably good electrical transport properties and present, in the monolayer limit, a direct band gap in the visible spectral range, especially appropriate for photodetectors and light-emitting devices.

In recent years, however, a growing interest has arisen for exploring and exploiting nonlinear optoelectronic effects (valley-Hall effect [8], photogalvanic and photon drag effects [9–11], photoexcited carrier funneling [12–14], etc) to achieve complex functionalities in 2D semiconductor devices. Such nonlinear effects are strongly linked with crystal symmetry and therefore, they are often absent in conventional, high-symmetry TMDs. Thus, in order to exploit these effects it is necessary to resort to low-symmetry layered materials, such as atomically thin black phosphorus [15, 16], Re-based TMDs [17–19], or 2D transition metal trichalcogenides. However, the optoelectronic properties of many of these materials are still not fully explored.

Among low-symmetry 2D materials, the family of group IV–V transition metal trichalcogenides (IV–V TMTCs) has recently attracted growing interest, mainly due to their quasi-1D electrical and optical properties stemming from a reduced in-plane structural symmetry. IV–V TMTCs are described by

the general formula of MX_3 being M a transition metal atom belonging to either group IVB (Ti, Zr, Hf) or group VB (Nb, Ta) and X chalcogen atoms from group VIA (S, Se, Te). The most deeply investigated atomically thin material in this family is few-layer TiS_3, which has shown promising optoelectronic properties for photodetection applications [12].

Here, we focus on $ZrSe_3$: a layered semiconductor of the IV–V TMTCs family with a strong in-plane anisotropic structure, similar to the one found in TiS_3. While experimental studies for this material are still very scarce, and its fundamental electronic and optical properties are not fully described in literature, recent studies have demonstrated its potential for nonlinear electronic and optoelectronic technologies. Xiong *et al* recently presented a photodetector based on individual $ZrSe_3$ nanobelts [20] and Zhou *et al* theoretically proposed its potential application for thermoelectrics [21]. In a previous work by our group [22], we found that the optical response of $ZrSe_3$ is extremely sensitive to uniaxial strain, showing strain gauge factors up to 95 meV $\%^{-1}$ for strain applied along the *b*-axis, which makes this material especially suitable for developing strain-tunable devices.

In this work, we explore the fundamental optical and optoelectronic properties of few-layer $ZrSe_3$, both at room temperature and in cryogenic vacuum. The $ZrSe_3$ optical spectra reveal a series of excitonic features, whose intensity is strongly modulated by the polarization of light. Even though similar spectral features can also be seen in photocurrent spectra, their relative intensity is markedly different from the ones obtained in the optical spectra. By comparing the two spectral measurements we can extract information on the contribution of optically generated excitons to photocurrent. Our work fills a gap of information in earlier literature and represents a required step towards exploiting the exotic symmetry and optical properties of atomically thin $ZrSe_3$ in nonlinear optoelectronic devices.

2. Device fabrication and characterization

$ZrSe_3$ crystallizes in a layered structure characterized by a strong in-plane anisotropy (see figures 1(a) and (b)). Each layer consists of Zr atoms coordinated with three Se atoms, forming chains of edge-sharing octahedra aligned along the *b*-axis. Individual layers are stacked along the *c*-axis, with relatively weak van der Waals forces holding the layers together. This allows for easy exfoliation into few-layer or monolayer forms. To fabricate the few-layer $ZrSe_3$ devices we make use of a combination of mechanical exfoliation and a deterministic placement technique [23]. figure 1(c) shows an optical microscopy image of a typical device. The few-layer $ZrSe_3$ is obtained by mechanical exfoliation with Nitto tape (SPV 224) from a bulk synthetic crystal
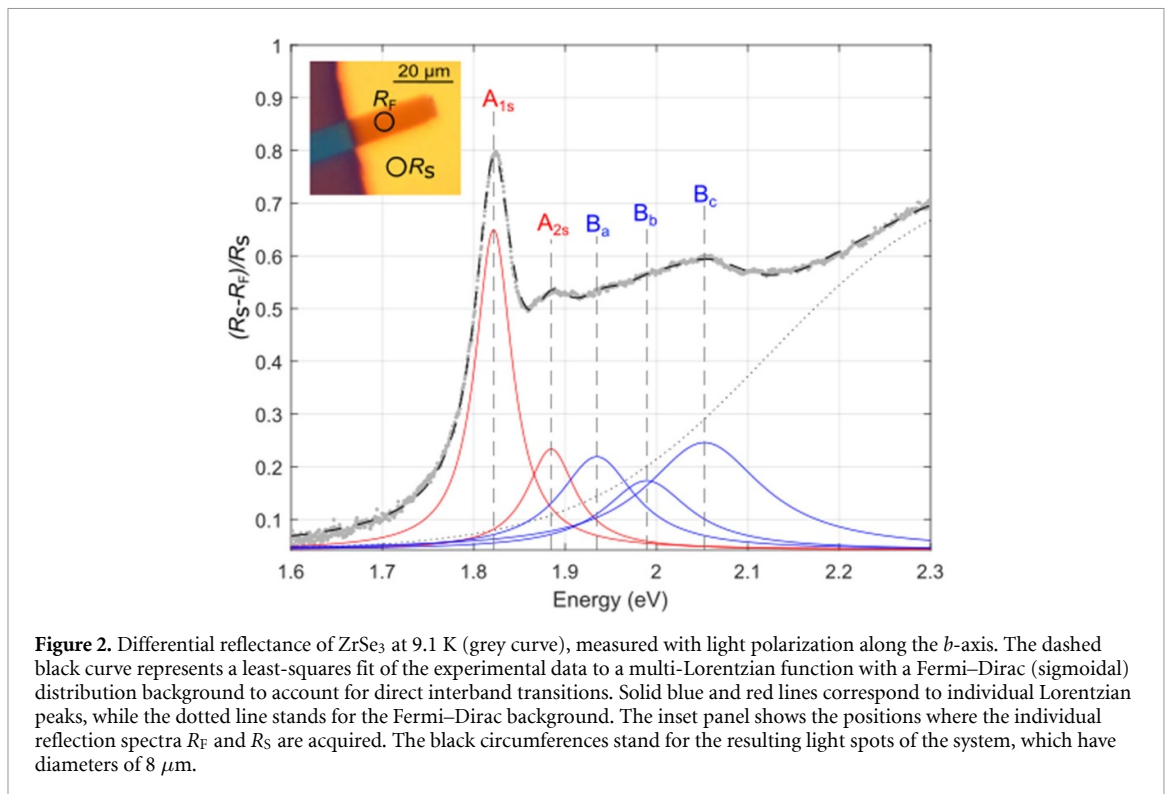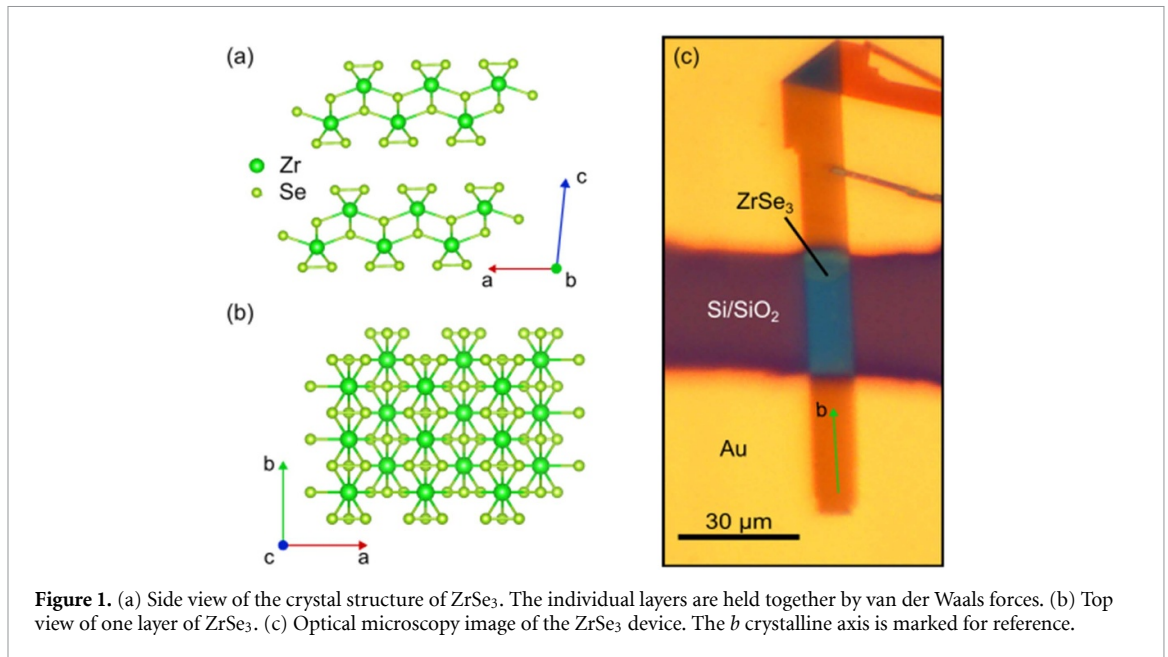
(purchased from HQ Graphene) onto a viscoelastic polydimethylsiloxane (PDMS) stamp from Gel-Pak® (Gel-Film WF x4 6.0mil). Then, we inspect the surface of the Gel-Film substrate by transmission-mode optical microscopy and identify atomically thin flakes by their faint optical contrast. Once a target flake is selected, we use the deterministic placement method described in [23]. to transfer it onto two Au/Ti electrodes, previously fabricated by optical lithography and e-beam evaporation, as further discussed in the methods section. Mechanical exfoliation of $ZrSe_3$ tends to produce long ribbon-shaped flakes, which their long edges parallel to the *b*-axis. This allows one to easily transfer $ZrSe_3$ flakes bridging two electrodes with their *b*-axis parallel to the electronic transport direction, as is indeed the case of the device presented in figure 1(c).

3. Optical response

We start our analysis by characterizing the optical response of $ZrSe_3$. We employ a home-made micro-reflectance system (fully described in section S3 of the Supp. Info.) to measure the differential reflectance spectrum of the $ZrSe_3$ flake on top of the gold electrode [24]. We define the differential reflectance $(R_S - R_F)/R_S$, with R_F being the reflected light of the $ZrSe_3$ flake and R_S that of the gold substrate. As further discussed in section S4 of the Supp. Info., this quantity qualitatively resembles the absorption spectrum of $ZrSe_3$. It is worth noting that spectral features in the differential reflectance spectra may be redshifted by roughly 20 meV compared to the corresponding peaks in absorption (also discussed in the Supp. Info.).

Figure 2 shows a spectrum acquired for the $ZrSe_3$ on top of the Au electrode. There, we discern two main peaks at 1.82 and 1.89 eV (highlighted in red) which we identify as the main exciton transition A_{1s} and its first excited state A_{2s}, respectively [25]. We also observe three additional peaks at higher energies, labeled in the figure as B_a, B_b and B_c. These peaks, also observed in earlier literature for cleaved $ZrSe_3$ crystals [25], are attributed to a second branch of excitonic states, as further discussed below. The experimental spectrum can be accurately fitted by an effective model including five individual Lorentzian distributions associated to the different excitonic peaks labeled in the figure, as well as a sigmoidal distribution that accounts for the smooth spectral background caused by impurity-mediated optical transitions near the bandgap.

We now turn our attention to the polarization dependence of the $ZrSe_3$ optical response. Figure 3(a) shows differential reflectance spectra acquired for illumination at different angles of polarization, relative to the *b* crystalline axis. There we observe how the optical response of $ZrSe_3$ is very strongly modulated by polarization, as also reported in earlier literature,

Figure 1. (a) Side view of the crystal structure of ZrSe$_3$. The individual layers are held together by van der Waals forces. (b) Top view of one layer of ZrSe$_3$. (c) Optical microscopy image of the ZrSe$_3$ device. The *b* crystalline axis is marked for reference.

Figure 2. Differential reflectance of ZrSe$_3$ at 9.1 K (grey curve), measured with light polarization along the *b*-axis. The dashed black curve represents a least-squares fit of the experimental data to a multi-Lorentzian function with a Fermi–Dirac (sigmoidal) distribution background to account for direct interband transitions. Solid blue and red lines correspond to individual Lorentzian peaks, while the dotted line stands for the Fermi–Dirac background. The inset panel shows the positions where the individual reflection spectra R_F and R_S are acquired. The black circumferences stand for the resulting light spots of the system, which have diameters of 8 μm.

both for few layer ZrSe$_3$ at room temperature [26] and for bulk ZrSe$_3$ at cryogenic temperature [25]. In particular, the five excitonic features described above disappear for light polarization perpendicular to the *b*-axis. This strong anisotropy is also illustrated in figure 3(b), where we present the polarization-dependent intensity of the A$_{1s}$ and A$_{2s}$ peaks, extracted from least square fittings like the one presented in figure 2. In particular, the intensity of A$_{1s}$ increases by a factor 40 when the light polarization is changed from perpendicular to parallel to the *b*-axis. The two first excitonic peaks reach their maximal intensity for

the same polarization angle, supporting our labeling of A$_{2s}$ as an excited state of A. In the case of B$_a$, B$_b$ and B$_c$ the maximal intensity is reached for a slightly different angle of polarization, between 10 and 20 degrees below the maxima of the A peaks (shown in Supp. Info. Section S5).

Lastly, it is also worth noting that while excitonic features are extremely sensitive to polarization, the smooth spectral background, which we attribute to direct interband transitions and/or absorption by bands of defect states, only shows a weak polarization dependence. For example, figure 3(c) shows that
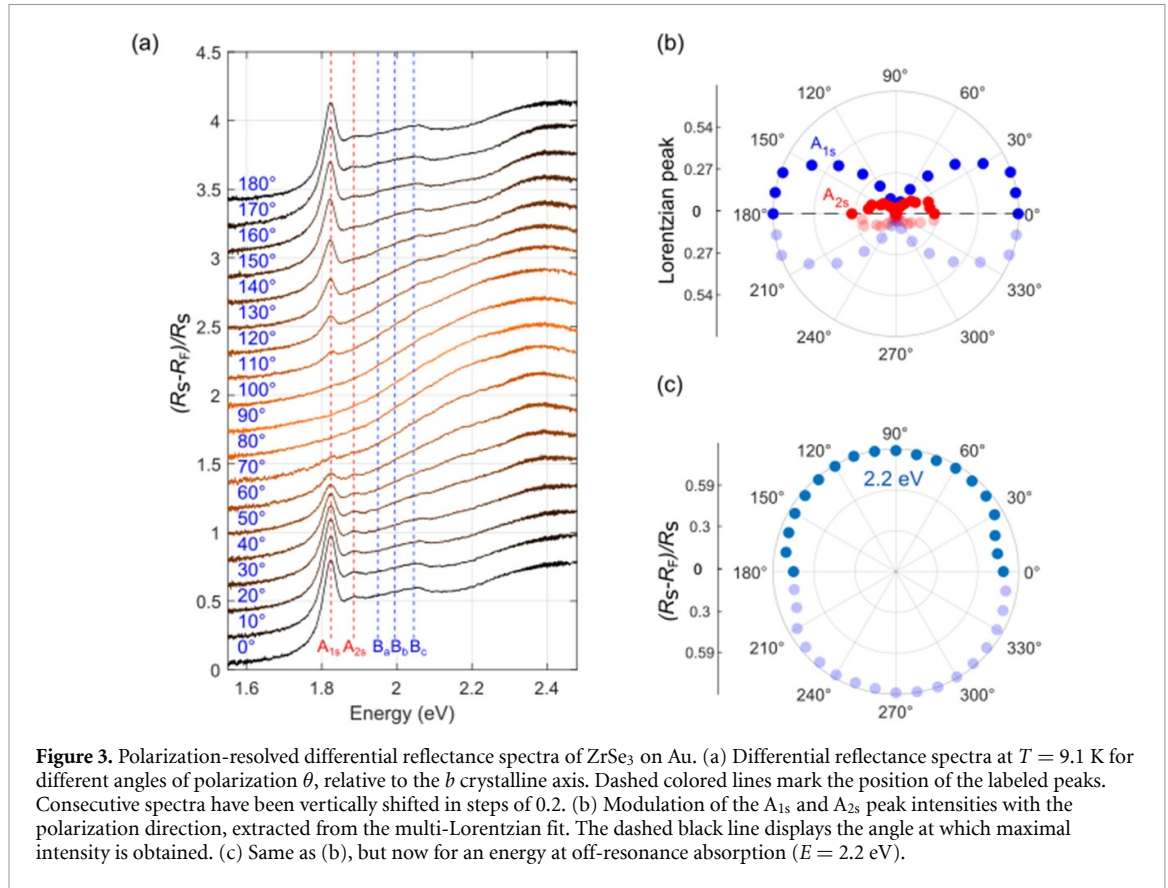
Figure 3. Polarization-resolved differential reflectance spectra of ZrSe$_3$ on Au. (a) Differential reflectance spectra at $T = 9.1$ K for different angles of polarization θ, relative to the b crystalline axis. Dashed colored lines mark the position of the labeled peaks. Consecutive spectra have been vertically shifted in steps of 0.2. (b) Modulation of the A$_{1s}$ and A$_{2s}$ peak intensities with the polarization direction, extracted from the multi-Lorentzian fit. The dashed black line displays the angle at which maximal intensity is obtained. (c) Same as (b), but now for an energy at off-resonance absorption ($E = 2.2$ eV).

for off-resonance absorption at 2.2 eV, the intensity changes only by a factor 1.16 when switching from perpendicular to parallel polarization.

We also analyzed the temperature dependence of the differential reflectance. Figure 4(a) shows a series of differential reflectance spectra acquired at different temperatures. As the temperature increases, excitonic peaks become progressively broadened and redshifted. The position of A$_{1s}$ peak is depicted in figure 4(b) as a function of temperature. The peak shifts by roughly 50 meV between 12 K and 300 K. This redshift has also been observed in other semiconductors and can be explained by the effect of thermally activated electron-phonon interactions which effectively decrease the optical bandgap. The temperature-dependent exciton energy A$_{1s}$ (T) can be modeled as [27, 28]

$$A_{1s}(T) = A_{1s}(0) - \frac{2a_B}{\exp(\Theta_B/T) - 1}, \qquad (1)$$

where a_B is the strength of the electron-phonon interaction, Θ_B is the average phonon temperature and A$_{1s}$ (0) is the exciton energy at $T = 0$ K. By fitting our experimental values for A$_{1s}$ to equation (1) we get $a_B = 17$ meV, comparable to the values obtained for other 2D materials [27, 28], and $\Theta_B = 152$ K, which is of the order of the Debye temperature $\Theta_D = 110$ K [29].
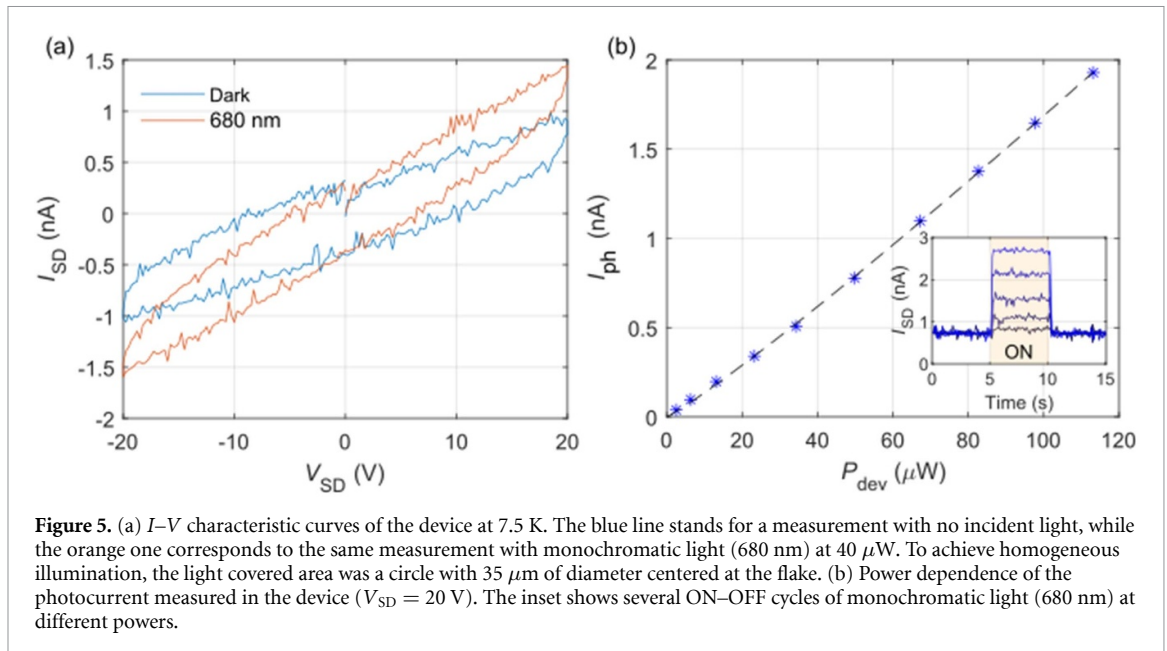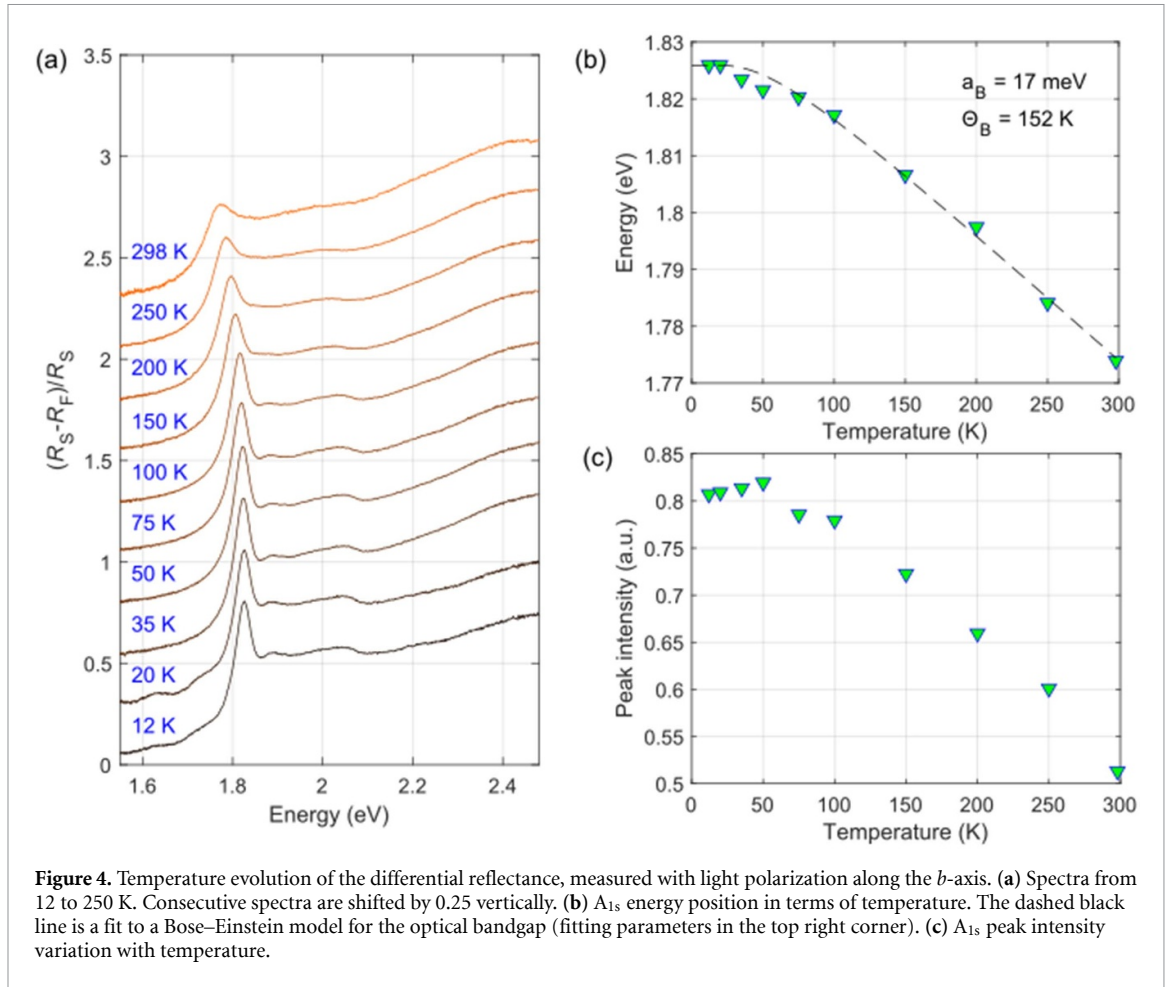
Besides shifting the peak positions, the presence of phonons is also expected to cause a decrease of

the exciton peak intensity with temperature, as it reduces the oscillator strength of the exciton absorption. As shown in figure 4(c), the intensity of A$_{1s}$ indeed decreases with temperature. However, as further discussed below, this decrease is only observed for temperatures above 50 K.

4. Optoelectronic response

We now turn our attention to the optoelectronic response of few-layer ZrSe$_3$. Figure 5(a) shows an I–V trace measured in the device shown in figure 1(c) at $T = 7.5$ K. The few-layer ZrSe$_3$ channel is highly resistive, with a conductance of roughly 50 pS. While we tried to apply a gate voltage to the Si/SiO$_2$ substrate to increase the carrier density in the channel, the electrical response of the device was unaltered for the available voltage range, both in the dark and under broadband optical excitation. The hysteresis could be explained by charge trapping by localized states present at the ZrSe3 material and electrode interfaces, leading to capacitive behavior.

While the I–V trace shows considerable hysteresis, the current increases linearly with the voltage, suggesting that only small Schottky barriers are present in the device. As also shown in figure 5(a), the device conductivity increases upon illumination. The inset panel in the figure shows a set of time traces of the source–drain current I acquired for different illumination intensities for an excitation wavelength of

Figure 4. Temperature evolution of the differential reflectance, measured with light polarization along the *b*-axis. **(a)** Spectra from 12 to 250 K. Consecutive spectra are shifted by 0.25 vertically. **(b)** A_{1s} energy position in terms of temperature. The dashed black line is a fit to a Bose–Einstein model for the optical bandgap (fitting parameters in the top right corner). **(c)** A_{1s} peak intensity variation with temperature.

Figure 5. (a) *I–V* characteristic curves of the device at 7.5 K. The blue line stands for a measurement with no incident light, while the orange one corresponds to the same measurement with monochromatic light (680 nm) at 40 μW. To achieve homogeneous illumination, the light covered area was a circle with 35 μm of diameter centered at the flake. (b) Power dependence of the photocurrent measured in the device ($V_{SD} = 20$ V). The inset shows several ON–OFF cycles of monochromatic light (680 nm) at different powers.

680 nm (1.82 eV) and $V_{SD} = 20$ V. From these measurements we can extract the power dependence of the photocurrent I_{ph} (figure 5(b)), defined as the increase in the source–drain current upon illumination. We find that I_{ph} increases linearly with the illumination power, yielding a responsivity $R = 17.04 \mu$A/W. The

linear power dependence observed here suggests that the main mechanism for photoresponse is the photoconductive effect [30]. The device presents a relatively fast response. From the inset panel in figure 5(b) we infer that the device is relatively fast, with a response time at least below our time resolution (100 ms).

Additionally, we obtain an external quantum efficiency of 0.002% for monochromatic light of 680 nm and a specific detectivity of $D^* = 3.4 \times 10^6$ Jones (measured on a separate ZrSe3 device. Further discussed in Supp. Info. Section S6).

Next, we investigate the spectral dependence of the responsivity R. We modulate the optical excitation at a frequency of 0.25 Hz and register the photocurrent while scanning the illumination photon energy within the visible and near-infrared range. Figure 6(a) shows a set of photocurrent spectra acquired in the ZrSe3 device at $T = 8.7$ K for different linear polarizations of the optical excitation. There, we observe a series of polarization-dependent exciton features, similar to the ones described in the optical spectra of figure 3(a). However, the relative intensities of the spectral features show significant differences: Firstly, all the exciton features are much more pronounced compared to the smooth out-of-resonance background. This suggests that excitonic states are much more strongly coupled to conduction electronic states than sub-gap localized states, leading to a stronger contribution to charge transport via exciton dissociation. Secondly, the A_{1s} and A_{2s} exciton peaks are observed here with similar intensities, while in optical measurements A_{1s} was much more pronounced. This is expected for responsivity spectra, as excited exciton states have a weaker binding energy, which facilitates dissociation into electron–hole pairs. Similarly to what occurred in the optical spectra of figure 3(a), excitonic spectral peaks are strongly modulated by polarization (shown in figure 6(b) for the A_{1s} peak). However, in the responsivity spectra the peaks are still visible even for polarization perpendicular to the b-axis. This phenomenon is particularly marked for B_c, which is only reduced by roughly a factor 2 for perpendicular polarization. Finally, following the parallelism with figures 3, figure 6(c) shows the polarization dependence of the responsivity at an off-resonance energy of 2.2 eV. Notably, while the reflectance measurements indicated weak polarization dependence for off-resonance excitation, becoming maximal for polarization perpendicular to the b crystalline axis, the off-resonance responsivity shows a much stronger modulation, increasing by roughly a factor 2, and becoming maximal for polarization parallel to the b axis. The detailed mechanisms responsible for this different polarization dependence are still unclear to us, but they could involve the presence of polarization-dependent photocarrier lifetimes and/or mobilities in ZrSe3. Alternatively, the off-resonance responsivity at 2.2 eV could include contributions from higher energy excitonic states.

5. Discussion

We have provided an in-depth characterization of the optical and optoelectronic properties of atomically thin ZrSe3. The presented micro reflectance spectra

reveal the presence of a strong absorption peak at 1.82 eV, labeled as A_{1s}. This feature, also observed in an earlier work by Kurita *et al* [25], is usually attributed to the formation of excitons at the Γ point of the reciprocal lattice. We observe an additional peak at 1.89 eV, $\sim$65 meV above A_{1s}, which we attribute to the first excited state of the A exciton, A_{2s}. This feature is not visible at temperatures above 200 K. Further, it is not reported in earlier literature for low-temperature optical spectroscopy. The absence of the A_{2s} peak in earlier literature for cleaved ZrSe3 could be explained by a difference in doping level and/or sample quality, which are known to strongly affect the optical response of excited excitonic states [31].

Besides A_{1s} and A_{2s}, we also observed three weak excitonic features at higher energies, which we labeled as B_a, B_b and B_c. Recent band structure calculations revealed that the two higher energy sub-bands at the valence band of ZrSe3 have an energy splitting of roughly 150 meV [26], compatible with the splitting between the A_{1s} peak and the B peaks observed in our spectra. Thus, we believe that these peaks are mainly produced by exciton states associated with transitions at the Γ point, between the second sub-band of the valence band and the edge of the conduction band. In this case, however, it is not possible to correlate the different peaks to individual energy levels, as they are not fully resolved in the spectra, and each peak may contain contributions from more than one excited state of the B exciton. Polarization-dependent optical measurements reveal that all the observed exciton peaks practically become maximal for polarization parallel to the b-axis, while fully disappearing for perpendicular polarization. The same trend is also observed in responsivity spectra. There, however, it is still possible to distinguish the excitonic features (specially B_c) even at perpendicular polarization, since they become much more intense than the smooth background.

As expected, when the temperature is increased the excitonic spectral features broaden and experience a redshift due to the presence of phonons. The intensity of exciton peaks is also reduced at higher temperatures. However, it seems to remain stable, or even slightly increase, from 10 K to 50 K. This could be explained if the interband transition at Γ is slightly indirect, as suggested by DFT calculations [22]. In this case, a nonzero density of phonons may provide the necessary momentum kick to facilitate optical transitions.

While the fast photoresponse and strong polarization sensitivity of the ZrSe3 devices presented here is promising from a technological perspective, we do not believe that this material alone would be a good candidate for development of photodetectors, as it shows a very weak responsivity compared to other atomically thin materials. While, in a recent work [32], authors have reported much higher responsivity values for ultrathin ZrSe3, the power dependence
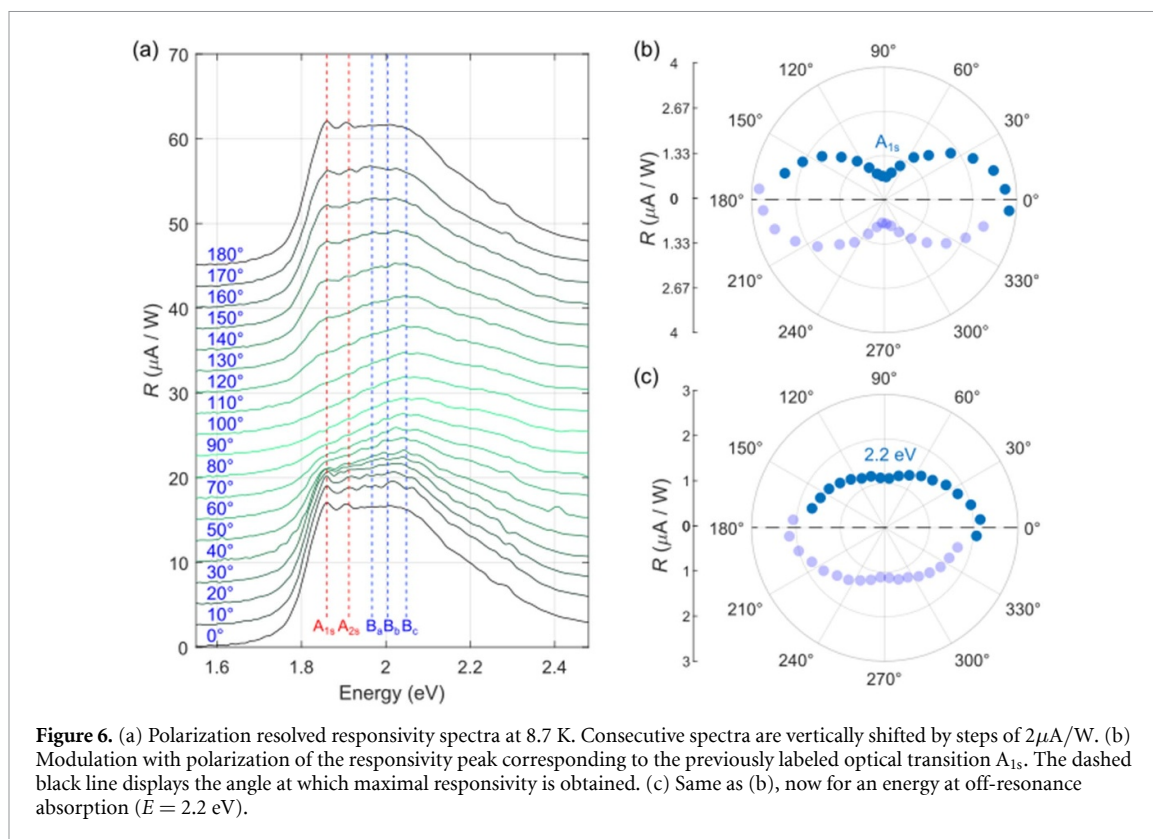
Figure 6. (a) Polarization resolved responsivity spectra at 8.7 K. Consecutive spectra are vertically shifted by steps of 2μA/W. (b) Modulation with polarization of the responsivity peak corresponding to the previously labeled optical transition A_{1s}. The dashed black line displays the angle at which maximal responsivity is obtained. (c) Same as (b), now for an energy at off-resonance absorption ($E = 2.2$ eV).

of their photodetectors showed a sublinear behavior, and these large responsivities were only achieved at extremely low illumination power, making it unsuitable for most technological applications. Further, the dichroic ratios obtained there only reached a maximum value of 1.1, while here we obtain dichroic ratios of up to 4 for illumination on resonance with the A_{1s} exciton peak. The behavior of their devices could be explained by the presence of metal-induced gap states at the electrode interfaces, leading to saturable photoresponse.

Nevertheless, the dichroic ratios obtained here for ZrSe$_3$ are among the strongest among polarization-dependent photodetectors based on 2D materials, comparable to the value recently reported for violet phosphorus devices [33] (3.9) and well above those obtained for other 2D materials such as ZrS$_3$ [34] (1.6) and Bi$_2$S$_3$ [35] (2.4), to name a few. Therefore, we believe that atomically thin ZrSe$_3$ could be used in combination with other materials, such as 2D TMDs, to fabricate hybrid devices that take advantage of its extremely anisotropic crystal symmetry and its light polarization sensitivity.

6. Methods

Device fabrication—The ZrSe$_3$ flakes located on the PDMS were characterized by optical transmission microscopy (Motic BA310 Met-T metallurgical microscope, equipped with a 18 megapixel digital camera AMScope MU1803 and a fiber-coupled compact spectrometer Thorlabs CCS200/M) with polarized light to determine the crystalline orientations, the polarized light was rotated in a counterclockwise direction to reach an angle of 0°–360° between the polarized light and the cleaved edge of the fixed sample, which is identified as θ. Then few-layered ZrSe$_3$ flakes were then transferred between pre-patterned Au/Ti electrodes (fabricated by electron-beam evaporation through a metal shadow mask from Ossila®) on Si/SiO$_2$ substrate by using an all-dry deterministic transfer method.

atomic force microscopy (AFM) characterization— A commercial AFM system, from CSI Instrument, operating in ambient conditions was employed to perform morphological characterization of the samples (see Supp. Info. Section S1). Measurements have been acquired in dynamic mode with silicon tips (PPP-FMR from Nanosensors). Image analysis was performed with the WSxM free software [36].

Low temperature optoelectronic characterization— Low temperature optoelectronic measurements were carried out in vacuum (10^{-5} bar) using an Attocube ATTO DRY800 system providing optical and electrical access to the samples and temperature control.

Data availability statement

All data that support the findings of this study are included within the article (and any supplementary files).

Author contributions

The manuscript was written through contributions of all authors. All authors have given approval to the final version of the manuscript.

Conflict of interest

The authors declare no competing interests.

ORCID iDs

Pedro L Alcázar Ruano ⬤ https://orcid.org/0000-0002-5350-9252
Estrella Sánchez Viso ⬤ https://orcid.org/0000-0003-0202-4340
Andres Castellanos-Gomez ⬤
https://orcid.org/0000-0002-3384-3405

References

[1] Koppens F H L, Mueller T, Avouris P, Ferrari A C, Vitiello M S and Polini M 2014 Photodetectors based on graphene, other two-dimensional materials and hybrid systems *Nat. Nanotechnol.* **9** 780–93

[2] Huang Z, Li Y, Zhang Y, Chen J, He J and Jiang J 2024 2D multifunctional devices: from material preparation to device fabrication and neuromorphic applications *Int. J. Extrem. Manuf.* **6** 032003

[3] Kang S, Lee D, Kim J, Capasso A, Kang H S, Park JW, Lee C H and Lee GH 2020 2D semiconducting materials for electronic and optoelectronic applications: potential and challenge *2D Mater.* **7** 022003

[4] Futures M *et al* 2024 Low-dimensional van der Waals materials for linear-polarization-sensitive photodetection: materials, polarizing strategies and applications *Mater. Future* **3** 12301

[5] Wang Q H, Kalantar-Zadeh K, Kis A, Coleman J N and Strano M S 2012 Electronics and optoelectronics of two-dimensional transition metal dichalcogenides *Nat. Nanotechnol.* **7** 699–712

[6] Radisavljevic B, Radenovic A, Brivio J, Giacometti V and Kis A 2011 Single-layer MoS_2 transistors *Nat. Nano* **6** 147–50

[7] Yin Z, Li H, Li H, Jiang L, Shi Y, Sun Y, Lu G, Zhang Q, Chen X and Zhang H 2012 Single-layer MoS_2 phototransistors *ACS Nano* **6** 74–80

[8] Mak K F, McGill K L, Park J and McEuen P L 2014 The valley Hall effect in MoS_2; transistors *Science* **344** 1489–92

[9] Eginligil M, Cao B, Wang Z, Shen X, Cong C, Shang J, Soci C and Yu T 2015 Dichroic spin-valley photocurrent in monolayer molybdenum disulphide *Nat. Commun.* **6** 7636

[10] Quereda J, Ghiasi T S, You J S, van den Brink J, van Wees B J and van der Wal C H 2018 Symmetry regimes for circular photocurrents in monolayer $MoSe_2$ *Nat. Commun.* **9** 3346

[11] Xie Y, Zhang L, Zhu Y, Liu L and Guo H 2015 Photogalvanic effect in monolayer black phosphorus *Nanotechnology* **26** 455202

[12] Island J O, Biele R, Barawi M, Clamagirand J M, Ares J R, Sánchez C, van der Zant H S J, Ferrer I J, D'Agosta R and Castellanos-Gomez A 2016 Titanium trisulfide (TiS_3): a 2D semiconductor with quasi-1D optical and electronic properties *Sci. Rep.* **6** 1–7

[13] Lei L *et al* 2020 Efficient energy funneling in quasi-2D perovskites: from light emission to lasing *Adv. Mater.* **32** 1–9

[14] Castellanos-Gomez A, Roldán R, Cappelluti E, Buscema M, Guinea F, van der Zant H S J and Steele G A 2013 Local strain engineering in atomically thin MoS_2 *Nano Lett.* **13** 5361–6

[15] Quereda J, San-Jose P, Parente V, Vaquero-Garzon L, Molina-Mendoza A J, Agraït N, Rubio-Bollinger G, Guinea F, Roldán R and Castellanos-Gomez A 2016 Strong modulation of optical properties in black phosphorus through strain-engineered rippling *Nano Lett.* **16** 2931–7

[16] Castellanos-Gomez A 2015 Black phosphorus: narrow gap, wide applications *J. Phys. Chem. Lett.* **6** 4280–91

[17] Wang Y Y, Zhou J D, Jiang J, Yin T T, Yin Z X, Liu Z and Shen Z X 2019 In-plane optical anisotropy in ReS_2 flakes determined by angle-resolved polarized optical contrast spectroscopy *Nanoscale* **11** 20199–205

[18] Aslan O B, Chenet D A, Van Der Zande A M, Hone J C and Heinz T F 2016 Linearly polarized excitons in single- and few-layer ReS_2 crystals *ACS Photonics.* **3** 96–101

[19] Chenet D A, Aslan B, Huang P Y, Fan C, van der Zande A M, Heinz T F and Hone J C 2015 In-plane anisotropy in mono- and few-layer ReS_2 probed by Raman spectroscopy and scanning transmission electron microscopy *Nano Lett.* **15** 5667–72

[20] Xiong W W, Chen J Q, Wu X C and Zhu J J 2015 Visible light detectors based on individual $ZrSe_3$ and $HfSe_3$ nanobelts *J. Mater. Chem.* C **3** 1929–34

[21] Zhou Z, Liu H, Fan D, Cao G and Sheng C 2018 high thermoelectric performance originating from the grooved bands in the $ZrSe_3$ monolayer *ACS Appl. Mater. Interfaces* **10** 37031–7

[22] Li H *et al* 2022 Strongly anisotropic strain-tunability of excitons in exfoliated $ZrSe_3$ *Adv. Mater.* **34** 37031–7

[23] Castellanos-Gomez A, Buscema M, Molenaar R, Singh V, Janssen L, van der Zant H S J and Steele G A 2014 Deterministic transfer of two-dimensional materials by all-dry viscoelastic stamping *2D Mater.* **1** 011002

[24] Frisenda R *et al* 2017 Micro-reflectance and transmittance spectroscopy: a versatile and powerful tool to characterize 2D materials *J. Phys. D: Appl. Phys.* **50** 074002

[25] Kurita S, Staehli J L, Guzzi M and Lévy F 1981 Optical properties of ZrS_3 and $ZrSe_3$ *Phys.* B+C **105** 169–73

[26] Li H *et al* 2022 Strongly anisotropic strain-tunability of excitons in exfoliated $ZrSe_3$ *Adv. Mater.* **34** 2103571

[27] Liu HLL, Yang T, Chen JH, Chen HW, Guo H, Saito R, Li MY and Li LJ 2020 Temperature-dependent optical constants of monolayer MoS_2, $MoSe_2$, WS_2, and WSe_2: spectroscopic ellipsometry and first-principles calculations *Sci. Rep.* **10** 15282

[28] Vina L, Viña L, Logothetidis S and Cardona M 1984 Temperature dependence of the dielectric function of germanium *Phys. Rev.* B **30** 1979–91

[29] Provencher R, Ayache C, Jandl S and Jay-Gerin J P 1986 Low-temperature specific heats of ZrSe3 and ZrS3 *Solid State Commun.* **59** 553–6

[30] Vaquero D, Clericò V, Salvador-Sánchez J, Díaz E, Domínguez-Adame F, Chico L, Meziani Y M, Diez E and Quereda J 2021 Fast response photogating in monolayer MoS$_2$ phototransistors *Nanoscale* **13** 16156–63

[31] Vaquero D, Clericò V, Salvador-Sánchez J, Martín-Ramos A, Díaz E, Domínguez-Adame F, Meziani Y M, Diez E and Quereda J 2020 Excitons, trions and Rydberg states in monolayer MoS$_2$ revealed by low-temperature photocurrent spectroscopy *Commun. Phys.* **3** 194

[32] Wang X, Xiong T, Xin K, Yang J, Liu Y, Zhao Z, Liu J and Wei Z 2022 Polarization sensitive photodetector based on quasi-1D ZrSe$_3$ *J. Semiconduct.* **43** 102001

[33] Liu H *et al* 2024 Polarization-sensitive photodetectors based on highly in-plane anisotropic violet phosphorus with large dichroic ratio *Adv. Funct. Mater.* **34** 1–8

[34] Chen F, Liu G, Xiao Z, Zhou H, Fei L, Wan S, Liao X, Yuan J and Zhou Y 2023 Quasi-ONE-DIMENSIONAL ZrS3 nanoflakes for broadband and polarized photodetection with high tuning flexibility *ACS Appl. Mater. Interfaces* **15** 16999–7008

[35] Yi H *et al* 2023 Quantum tailoring for polarization-discriminating Bi2S3 nanowire photodetectors and their multiplexing optical communication and imaging applications *Mater. Horizons* **10** 3369–81

[36] Horcas I, Fernández R, Gómez-Rodríguez J M, Colchero J, Gómez-Herrero J and Baro A M 2007 WSXM: a software for scanning probe microscopy and a tool for nanotechnology *Rev. Sci. Instrum.* **78** 013705